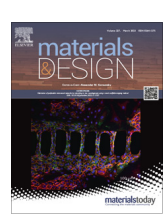
ELSEVIER

Contents lists available at ScienceDirect

Materials & Design

journal homepage: www.elsevier.com/locate/matdes



Process control of electrospinning artificial fenestrated capillary vessels



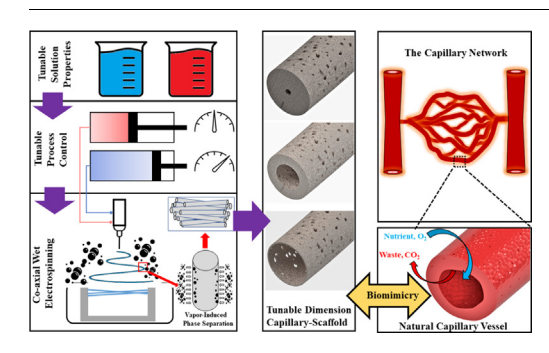
Imtiaz Qavi, George Tan*

Department of Industrial, Manufacturing, and Systems Engineering, Texas Tech University, Lubbock, TX 79409, USA

HIGHLIGHTS

- Porous polycaprolactone microtubes were fabricated by wet co-axial electrospinning. The outside diameters of the microtubes ranged from 2 to 5 µm. The inside diameter ranged from 0.5 to 4.5 µm. The average pore size ranged from 0.01 to 0.1 square µm. The geometry of these porous microtubes is similar to human fenestrated capillaries.
- The flow rate ratio of the core/sheath solutions and the viscosity of the sheath solution play a significant role in the outside diameter and inside diameter of the microtubes.
- The formation of surface pores is dominated by the humidity during the electrospinning. At the same humidity level, the size of the surface pores is positively correlated with the viscosity of the sheath solution and the outside diameter of the microtubes.
- Regression models with high R square values were built to quantify the relationship between process parameters and microtube geometric attributes.
- These artificial fenestrated capillaries can be used to facilitate vascularization in scaffolds for tissue engineering.

GRAPHICALABSTRACT



ARTICLE INFO

Article history: Received 20 December 2022 Revised 30 January 2023 Accepted 5 February 2023 Available online 11 February 2023

Keywords: Coaxial electrospinning

* Corresponding author.

E-mail address: george.z.tan@ttu.edu (G. Tan).

ABSTRACT

Rapid fabrication of capillary vessels is important for tissue engineering because local perfusion and oxygen exchange within the tissue depend on the network of capillaries which have diameters ranging from 5 to 10 µm. Fenestrated capillaries are microvessels that have surface pores of 80 to 100 nm in diameter. These capillaries are essential for many organs, such as small intestines, endocrine glands, and kidneys. In this paper, we presented a wet coaxial electrospinning technique for the rapid fabrication of porous microtubes as artificial fenestrated capillaries using polycaprolactone and polyethylene oxide. We characterized the effects of process parameters on the morphological features of these microtubes by

Nanoporous microtubes Artificial capillaries Vessel biofabrication Phase seperation Process optimization regression modeling. Our study shows that the flow rate ratio of the core/sheath solutions and the viscosity of the sheath solution play a significant role in the outside diameter, wall thickness, and hollow area of the microtubes. In addition, the formation of surface pores is dominated by the humidity during the electrospinning. At the same humidity level, the size of the surface pores is positively correlated with the viscosity of the sheath solution and the outside diameter of the microtubes. Overall, this study established the process-property relationship for wet coaxial electrospinning of artificial fenestrated capillaries.

© 2023 The Author(s). Published by Elsevier Ltd. This is an open access article under the CC BY-NC-ND license (http://creativecommons.org/licenses/by-nc-nd/4.0/).

1. Introduction

Tissue engineering is an interdisciplinary field that aims to produce functional replacement tissues for clinical use through the development of biological substitutes. Advanced manufacturing has enabled the rapid fabrication of three-dimensional (3D) biological constructs for tissue engineering. One of the main challenges for biofabrication is to create architectures with microvascular networks as natural tissues. While blood flow and macro-level perfusion can be achieved by artificial channels which mimic arteries and veins, local perfusion and oxygen exchange within the tissue depend on the network of capillaries which have diameters ranging from 5 to 10 µm [1]. Blood circulation via the microvascular network is essential for the survival of cells in many engineered tissues [2]. Typically cells reside within a range of 200 µm from capillaries where the diffusion of oxygen is sufficient for the cellular viability in the tissue mass [3]. The absence of a vascular network in a large 3D scaffold may lead to necrosis [4] and eventually local or global tissue failure.

Cell-laden scaffolds with perfusable channels can be fabricated by inkjet or extrusion bioprinting [5–7]. For example, endothelial and stem cells can be incorporated into a multilayered coaxial extrusion system and printed into highly organized vessels [8-10]. However, the nozzle size hindered the fabrication of features smaller than 100 μm. Stereolithography [11–14] and photolithography [15-20] can print vascular channels and networks in polymer with high resolution. The channel widths range from 50 µm to 1 mm. Two-photon photocrosslinking was able to fabricate a tubular structure [21,22] with an inner diameter of 18 μ m [23]. In addition, 4D bioprinting was also adopted to fabricate selffolding tubes [24,25] with internal diameters as small as 20 µm [26]. Despite the high resolution, the low fabrication efficiency of these processes limits their manufacturing scalability and the feasibility of creating centimeter-sized scaffolds. Rapid fabrication of capillary vasculatures, which have diameters ranging from 5 to 10 μm, is a critical and yet unsolved challenge.

Electrospinning is a process for generating micro/nanofibers from polymer solutions [27]. In this process, a polymer solution is subjected to a high electric potential which causes jetting, bending, stretching, and thinning of a polymer jet. A variety of electrospinning configurations have been developed in the last two decades to fabricate biomimetic scaffolds for nerves [28], musculoskeletal tissues [29,30], myocardium [31], and large vessels [32]. Coaxial electrospinning adopts a dual-material system that generates a concentric fiber structure through a nested spinneret [33]. This configuration can be used to fabricate tubular structures by choosing a dissolvable sacrificial material as the core material [34]. Zhou et al. conducted coaxial electrospinning in a humid environment to create core-sheath microfibers with surface pores due to the phase separation between water vapor and organic solvent in the sheath solution [35,36]. Porous polycaprolactone microtubes were obtained after the sacrificial cores were dissolved in water. With proper solution viscosity, electrospinning distance, and operating voltage, the outside diameter of these microtubes was controlled under 10 µm [37]. This technique was used to prepare microvessels in a polydimethylsiloxane microfluidic device PDMS as a blood-brain-barrier (BBB) model [38]. Compared to many photopolymer-based microfabrication methods, the main advantage of coaxial electrospinning is its high fabrication efficiency. Coaxial electrospinning can create a thin mat of microtubes over tens of square centimeters within several minutes.

Prior studies have demonstrated the feasibility of the rapid fabrication of porous microtubes by coaxial electrospinning. However, it is not clear how the wall thickness and the surface pores of the microtubes can be adjusted to achieve different vascular structures for specific functions. There is a knowledge gap in the controllability of microtube morphology which needs to be filled. In this paper, we comprehensively evaluated the effects of material and process factors on the morphological characteristics of microtubes fabricated by coaxial electrospinning. Biocompatible polycaprolactone (PCL) and polyethylene oxide (PEO) were used to prepare the polymer solutions at different concentrations. We hypothesized that the ratios of solution viscosity and flow velocity ratio between the core solution and the sheath solution dominate the structural features of the microtubes, including outside diameter, wall thickness, and pore size. We conducted the parametric study by varying the combination of core/sheath solutions and the flow rates of the electrospinning process and then performed a quantitative image analysis to characterize the morphological features of microtubes. Regression models were built based on statistical analysis. The results will lay the foundation for elucidating the formation mechanisms of nanopores and guide the optimization of microtube morphology for desirable biological functions.

2. Materials and methods

2.1. Polymer solutions

PCL with molecular weight (MW) = 80,000 (Sigma-Aldrich®, St. Louis, MO) and PEO with MW = 300,000 (Sigma-Aldrich®, St. Louis, MO) were used as the sheath and core polymers, respectively. Both the core and sheath polymers were dissolved in dichloromethane (DCM, \geq 99.5 %). The polymer solution was homogenized through magnetic stirring-induced agitation for 4 h at room temperature. Four combinations of different concentrations of the core and sheath solutions were tested as shown in Table 1.

Table 1Core and Sheath Solution Combinations.

Core: PEO in DCM (w/v)	Sheath: PCL in DCM (w/v)	Core to Sheath Concentration Designation
3 %	10 %	X1
6 %	10 %	X2
3 %	12 %	X3
6 %	12 %	X4

2.2. Electrospinning configuration

The core-sheath electrospinning operation was performed using a TL-Pro-BM robotic Electrospinning platform (Tongli Tech, China). A core-sheath coaxial spinneret was used to fabricate the hollow tubular microtubes as shown in Fig. 1. A dual syringe pump was used to pump the core and sheath polymer solution into the core-sheath coaxial spinneret. The core and the sheath needles used were gauges 26 and 20, respectively. At the tip of the needle, the Taylor cone was formed with the PEO solution in the center (red) enclosed by the PCL solution (blue) as shown in Fig. 1. A 3D-printed parallel plate collector with an adjustable gap was used to collect the fibers. The parallel plates were covered with aluminum foil to make them conductive. The gap was adjusted to an optimal level to ensure the collection of aligned fibers between the parallel plates. The parallel plate collectors were connected to the ground, and the spinneret was connected to a positive voltage terminal. In all the experiments, the positive voltage in the spinneret was kept constant at 8.5 kV, which was the minimum required potential required to initiate the whipping instability in the electrospinning jet.

The distance between the parallel plate collector and the spinneret was maintained at 12 cm for all the experiments. This is the minimum distance required to maintain a whipping effect for all the core-sheath combinations used in the current experiment. The entire chamber was kept closed during the experimentation and the humidity level was maintained at approximately 60–65% in all cases. The aligned fibers were collected between the parallel plates for 5 min after which they were collected on sticky tape. The tape ensured that the fibers were held tight in position and would not experience any further deformation from handling. The fibers were then soaked in a bath of liquid nitrogen for 3 min and dissected along the cross-section while in the nitrogen bath. Following the dissection, the fibers were submerged in deionized (DI) water for 1 h to remove the water-soluble PEO cores of the dual-material fibers.

In this study, the effect of varying volumetric flowrate on coreto-sheath linear flow velocity ratio within the spinneret needle was tested. The standard volumetric flowrate was determined to be the flowrate that produced an equal linear velocity of both core and sheath solutions in the concentric spinneret. In the standard condition, the core and sheath were expected to eject simultaneously from the needle. The flowrates were calculated based on the following equation:

$$\frac{Q_1}{Q_2} = \frac{A_1 * V_1}{A_2 * V_2} = \frac{\left(r_{1,i}^2\right) * V_1}{\left(r_{2,i}^2 - r_{1,o}^2\right) * V_2} \tag{1}$$

where, Q₁, Q₂, A₁, A₂, V₁, and V₂ are the volumetric flow rate, area of the spinneret cross-sectional opening, and average linear flow velocity within the spinneret needle of the core and sheath solutions, respectively. The radius variables $r_{1,i}$ and $r_{1,o}$ corresponds to the inner and outer spinneret radius of the core spinneret needle. The radius r_{2,i} corresponds to the inner radius of the sheath spinneret needle. The spinneret radii do not change in the current experiment. Hence A_1 and A_2 are constants with $A_1/$ $A_2 = 0.7$ (approximately). To ensure the full encapsulation of the core by a sheath in the Taylor cone, it is important to maintain a constant velocity of the ejecting core and sheath solutions. In other words, the core-sheath velocity ratio (CSVR) needs to be 1:1. According to equation (1), the core-sheath velocity ratio (CSVR) = 1:1 when the volumetric flowrates of the core and the sheath are 1.50 and 2.10 ml/h, respectively. The CSVR of 1:1 was set as the 'standard' value in this study.

We further explored the core/sheath encapsulation at different CSVR by adjusting the volumetric flowrate. Briefly, the core volumetric flowrate was held fixed at 1.5 ml/h while the sheath volumetric flowrate was adjusted to obtain a high CSVR of 1:0.5 and low CSVR of 1:2 and 1:3. The setting of the flowrates are summarized in Table 2.

2.3. Fluidic property measurements

The viscosity of the polymer solutions was measured using an MCR 92 Modular Compact Rheometer (Anton Paar, Austria). The viscosities were measured with shear rates ramping up from 0.1/s to 1000/s. A parallel plate rotary sampler of diameter 25 mm was used to measure the viscosity of all the solutions. The viscoelastic measurement model for the selected polymer solutions.

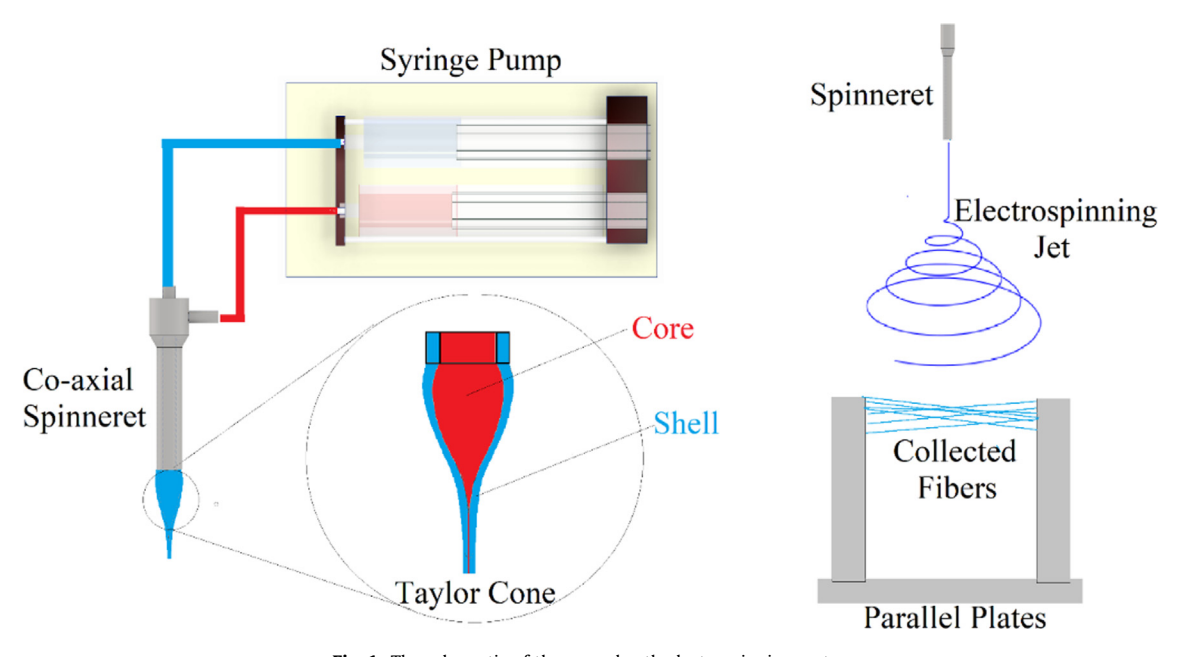


Fig. 1. The schematic of the core-sheath electrospinning system.

Table 2 Flow rates and core-to-sheath FVR of the core and sheath solutions.

Core Flowrate (ml/h)	Sheath Flowrate (ml/h)	Core-to-Sheath Volumetric Flow ratio	Core-to-Sheath Velocity Ratio (CSVR)
1.5	1.07	1:0.7	1:0.5
1.5	2.10	1:1.4	1:1*
1.5	4.29	1:2.8	1:2
1.5	6.40	1:4.2	1:3

^{*} Standard CSVR.

A Theta-Lite tensimeter (Biolin Scientific, Sweden) was used to measure the surface tension of the polymer solutions. A droplet of the polymer solution was suspended from a microneedle (gauge 28). The droplet was allowed to grow to 4.5 μ L in volume. Once the target volume of the droplet was reached, the tensiometer camera captured a sample of 50 images for each of the solutions at 8.7 frames/second. The surface tension was determined from the pendent droplet using OneAttension (Biolin Scientific, Sweden) built-in shape/size analyzer for surface tension measurements.

2.4. Microtube visualization and analysis

The microtube cross-section samples were sputter-coated with gold and then inspected by a scanning electron microscope (SEM) (Phenom Pro, Nanoscience, Phoenix, AZ). The nanopores were inspected by the field-emission SEM (Zeiss Crossbeam 540, Oberkochen, Germany). The analysis of microtube images was performed by Image] (National Institute of Health, USA). The original images were first converted to 8-bit images. Contrast-based thresholding was performed to identify the hollow crosssectional area or the surface pores, which appeared dark compared to the external portion of the fiber. The identified dark-contrast zones were automatically selected. A mask was generated from the selected image where the noises appeared as white dots. The noises could interfere with the cross-sectional area or pore size measurements. The noises were then eliminated using the binary processing "Fill hole" tool in ImageJ. Subsequently, the areas of the pores and sheath substrate were selected respectively based on the contrast using the Region-of-Interest (ROI) tool in the ImageJ software.

2.5. Statistical analysis

The experimental results were analyzed using the Wilcoxon test followed by the Kruskal-Wallis test. Both tests are suitable for non-parametric data sets.

3. Results and discussion

3.1. Viscosity and surface tension

The viscosity and surface tension are shown in Fig. 2. All the polymer solutions showed a shear-thinning property. We compared the viscosity values of the polymer solutions at a shear rate of 1000/s which is typical in electrospinning jets [39–41]. At a shear rate of 1000/s, 3 % PEO in DCM showed the lowest viscosity of 93 MPa·s. 10 % PCL in DCM showed a viscosity of 287 MPa·s. 6 % PEO and 12 % PCL in DCM showed a close viscosity level of around \sim 850 MPa·s.

Table 3 summarizes the ratio of core and sheath viscosities compared at the same shear rate of 1000/s for each of the coresheath concentration configurations tested:

The surface tension value of a pendent droplet was calculated using the following equation [42]:

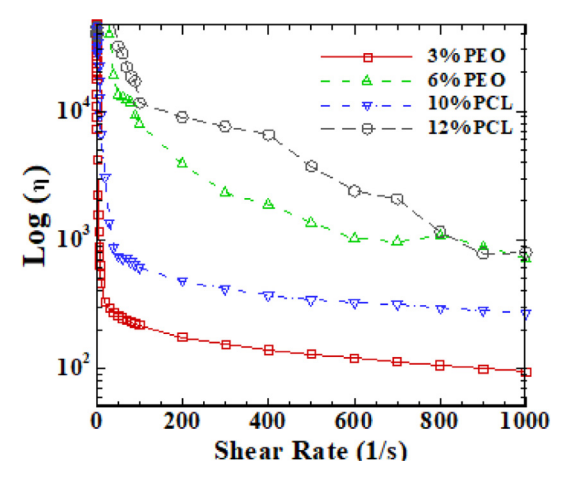


Fig. 2. Shear rate vs viscosity curve of the core and sheath polymer solutions.

Table 3Showing viscosity ratio of core/sheath solutions for each concentration combination.

Core Sheath Concentration Designation	Core Concentration	Sheath Concentration	Core-to-Sheath Viscosity Ratio
X1	3 %	10 %	1:3
X2	6 %	10 %	3:1
X3	3 %	12 %	1:9
X4	6 %	12 %	1:1

$$\gamma = \Delta p g \frac{R_o^2}{R} \tag{2}$$

where γ is the surface tension of the pendant droplet. Δp is the difference in density of the droplet and surrounding air. The gravitational constant is defined by g. R_o denotes the radius of curvature at the apex as shown in Fig. 3a. The shape factor (β) is obtained from the equations shown in Fig. 3a. The equations used to obtain the shape factor are based on the Young-Laplace shape factor analysis method [43]. Fig. 3a shows the transient surface tension curve of 3 % PEO in DCM. The surface tension stabilized after 7 s from the droplet initiation. The data curves of all polymer solutions stabilized after 7 s. Therefore, the surface tension in the stable region was used for comparing different polymer solutions.

The surface tension of the PCL and PEO show an increasing trend with the increase in polymer concentration in DCM as seen in Fig. 3b. This is consistent with previous literature that concludes the solute molecular interactions with the solvent lead to increased surface tension with an increase in polymer solution concentration [44,45]. The Tukey post-hoc test shows that the surface tension of 6 % PEO in DCM significantly varies from the other groups (p < 0.001).

3.2. Microtube electron microscopic images

The cross-section SEM images are shown in Fig. 4. The image in each row corresponds to the groups X1 to X4 with different core/ sheath concentration ratios as shown in Table 1. Each column of the images represents a particular CSVR of the core and sheath polymer solutions. For groups X1 and X3 at a flow rate ratio of 1:0.5, no tubular structure was formed. This structure was characterized by an open sheath that failed to fully encapsulate the core polymer solution. Group X1 and X3 had the same core solution concentration of 3 % PEO in DCM. In both cases, the viscosity of the core was greater than the viscosity of the sheath as seen in Table 3. Under a similar CSVR, groups X2 and X4 formed well-

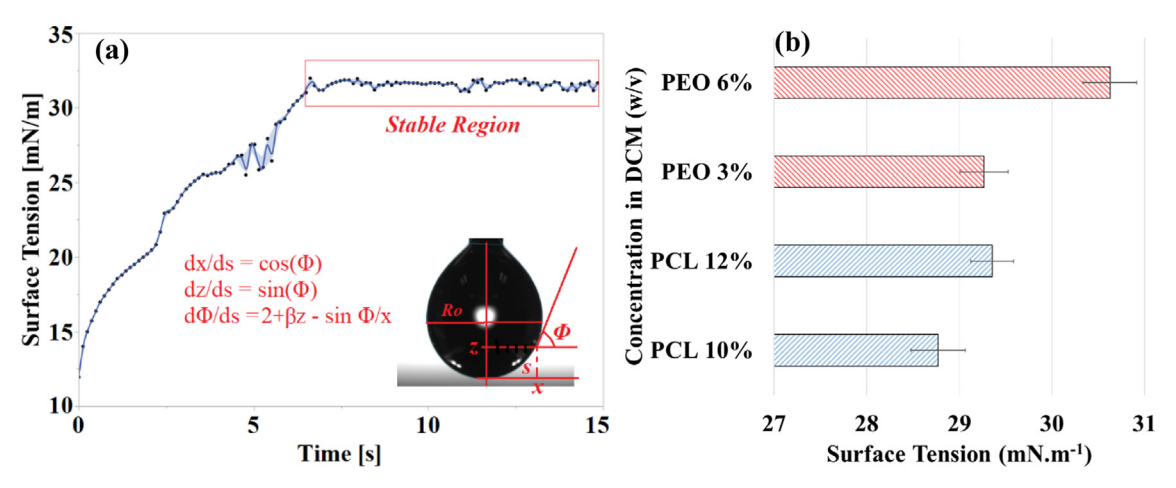


Fig. 3. Showing (a) Pendent droplet transient surface tension and shape factor analysis geometry (b) Surface tension values for the experimental core and sheath polymer solutions.

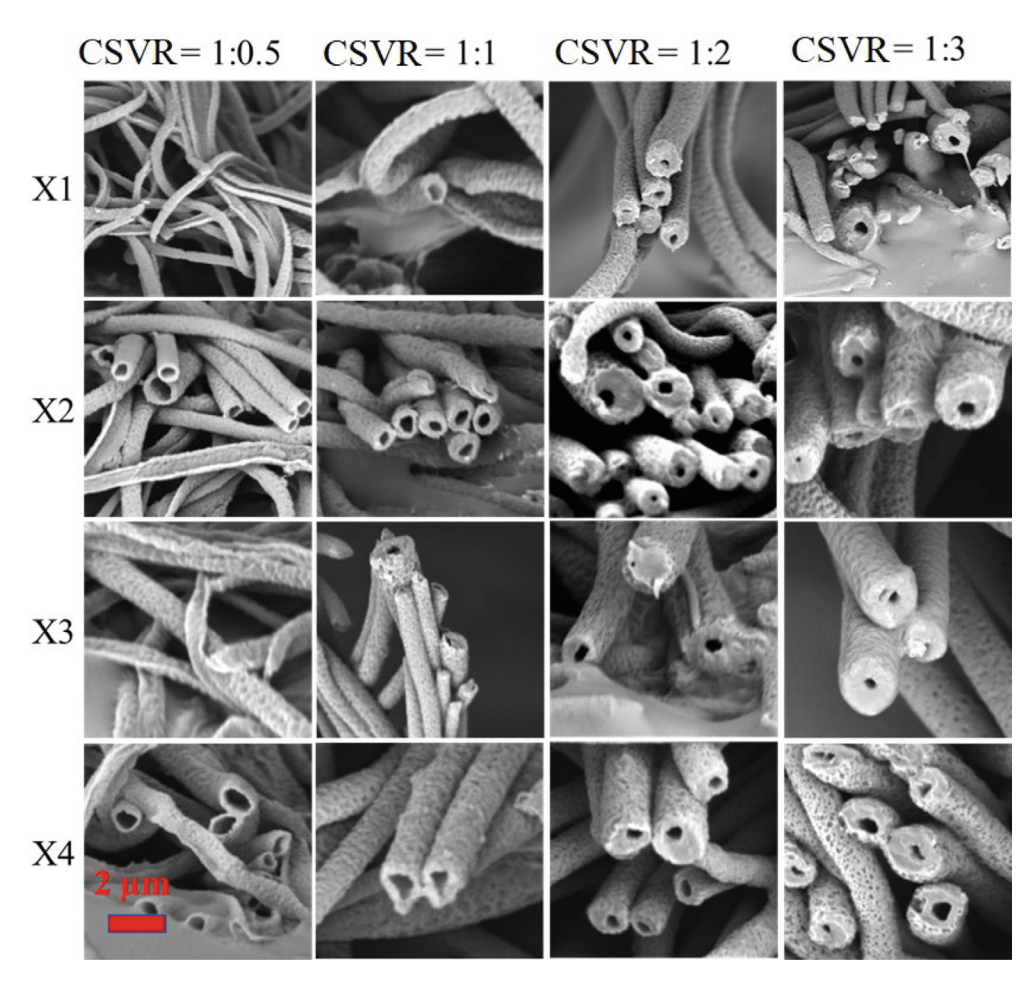


Fig. 4. Fiber cross-sectional image for different core-sheath concentration and flow rate ratios. Each row (X1 (3% core, 10% sheath), X2 (6% core, 10% sheath), X3 (3% core, 12% sheath), and X4 (6% core, 12% sheath)) refers to a solution concentration summarized in Table 1. Each column refers to a CSVR summarized in Table 2.

defined tubular structures bearing a core solution concentration of 6 % PEO in DCM. This result shows that surface tension and viscosity have a substantial influence on core/sheath structure encapsulation.

First, due to the significantly higher surface tension of the 6 % core solution, there exists an interfacial tension between the core and sheath polymer solutions [46]. The miscibility of the core and sheath solution is influenced by that interfacial surface tension

[47]. When the PEO concentration was low (3 %), the interfacial tension between the core and sheath solutions became weak. Therefore, the core and the sheath solutions started mixing in the jet. This resulted in open sheaths in the thin-walled fibers produced at a low sheath flowrate at CSVR = 1:0.5. When we used 6 % PEO core with 10 or 12 % PCL sheath, there was an adequate interfacial tension between the core and sheath to resist full mixing and form closed microtubes. This interfacial tension facilitated the for-

mation of the thin-walled encapsulation structures at the substandard CSVR of 1:0.5. Hence, at a low sheath flow rate, the formation of thin-walled microtubes is possible only when the core solution does not mix with the sheath solution in the spinning jet.

Second, the viscosity ratio between the core and sheath solution is another factor that influences sheath encapsulation. A similar phenomenon of incomplete encapsulation was observed for poly (lactic acid)/chitosan core/sheath nanofibers when the low sheath flow rate caused instability of the primary jet and failed encapsulation [48]. When the viscosity of the sheath is higher than the core, the increased viscous drag by the sheath on the core results in a full encapsulation of the jet as seen in configurations of X2 and X4 at CSVR of 1:0.5. Prior literature shows that sheath viscosity needs to be equal/higher than the core to overcome the interfacial surface tension forces that act at the boundary of the core/sheath solution in the jet [49,50]. Otherwise, uneven core/sheath structures are formed [49]. This theory is consistent with our observation of open sheaths at CSVR of 1:0.5 for X1 and X3. Our conjecture is that the uneven core/sheath structure causes a rupture in the thin sheath wall and forms an open sheath when the sheath flow velocity is low and the core viscosity is greater than the sheath viscosity, with the change in CSVR towards higher sheath flowrates for any concentration configuration, the fiber wall thickness, and overall fiber diameter increase. An increase in sheath flow rate increases the volumetric amount of sheath material going into the jet [48,51], and thus results in a thicker shell in the solidified fibers.

The tube surface morphology SEM images are shown in Fig. 5. In configuration X1, there is no visible surface pore below CSVR of 1:3. Instead, the surface is full of dents and wrinkles. Visible submicron-sized pores are visible in concentration configurations X2 through X4 when the CSVR is at or above 1:1. Literature shows that formation or wrinkle on fiber surface depends on the jet drying time (t_d), jet buckling time (t_b), hydrophobic nature of the solvent, and the rate of solvent evaporation [52–55]. For a highly volatile solvent, initially, a thin solid layer is formed at the surface of the jet [53]. Eventually, buckling instability causes surface deformation to form a wrinkled surface [53]. Drying time is the time needed to form solid fiber from the liquid jet [54]. The drying time is proportional to the fiber diameter. If $t_d \approx t_b$, wrinkles are formed [55]. Usually, Fiber diameter is proportional to the solution viscosity and flow rate [56]. X1 represents the set of core and sheath solutions with the lowest viscosity (for both core and sheath). Hence, fibers formed in this range have the lowest drying time as a result of a smaller jet diameter compared to the other groups. Hence, we assume that a solid surface is formed owing to faster jet drying time which impedes the diffusion of water molecules from the atmosphere. Also, the jet simultaneously undergoes buckling to form wrinkled surfaces rather than porous surfaces. The number of surface pores increases as the solution concentration and flow rate ratio increase. As the CSVR and concentration increase, the fiber diameter increases. The increase in diameter causes the jet to have longer t_d and thus more time for non-solvent vapor to diffuse into the sheath jet.

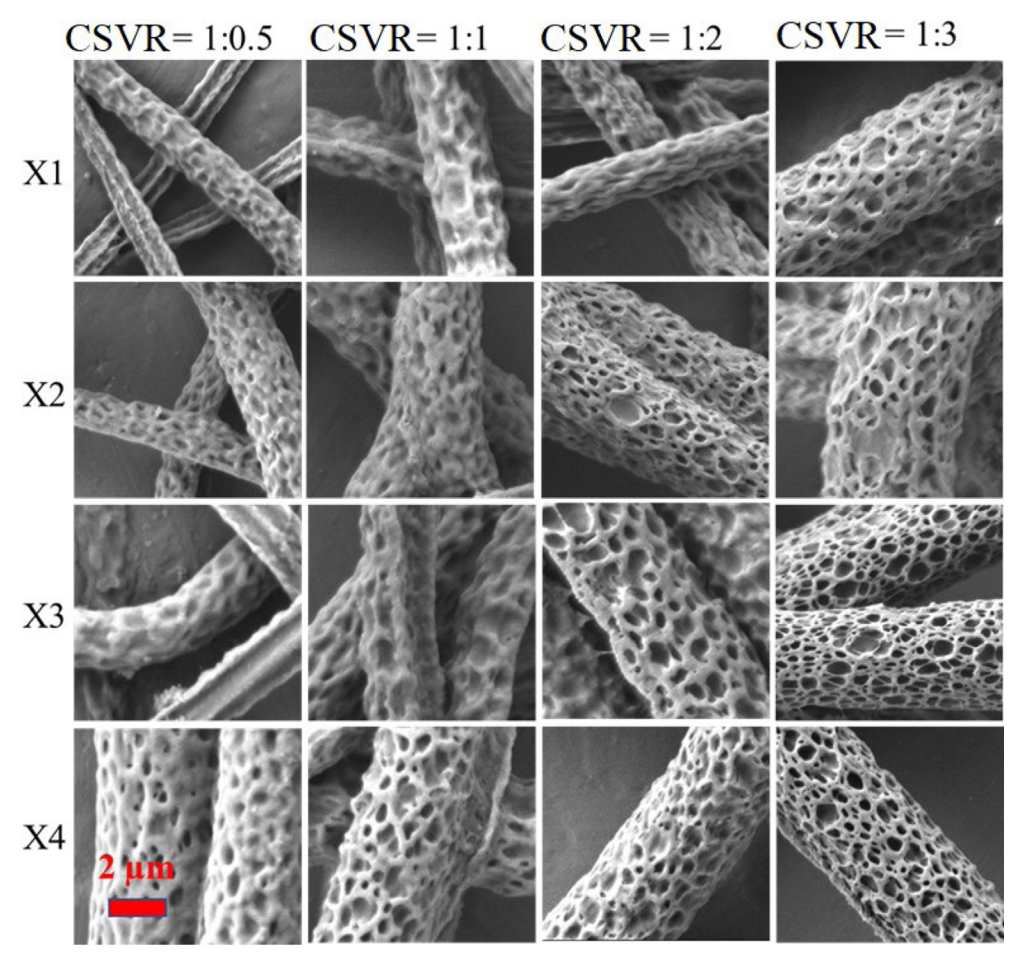


Fig. 5. Surface pore SEM image for different core-sheath concentrations and flow rate ratios. Each row (X1 (3% core, 10% sheath), X2 (6% core, 10% sheath), X3 (3% core, 12% sheath), and X4 (6% core, 12% sheath)) refers to a solution concentration summarized in Table 1. Each column refers to a CSVR summarized in Table 2.

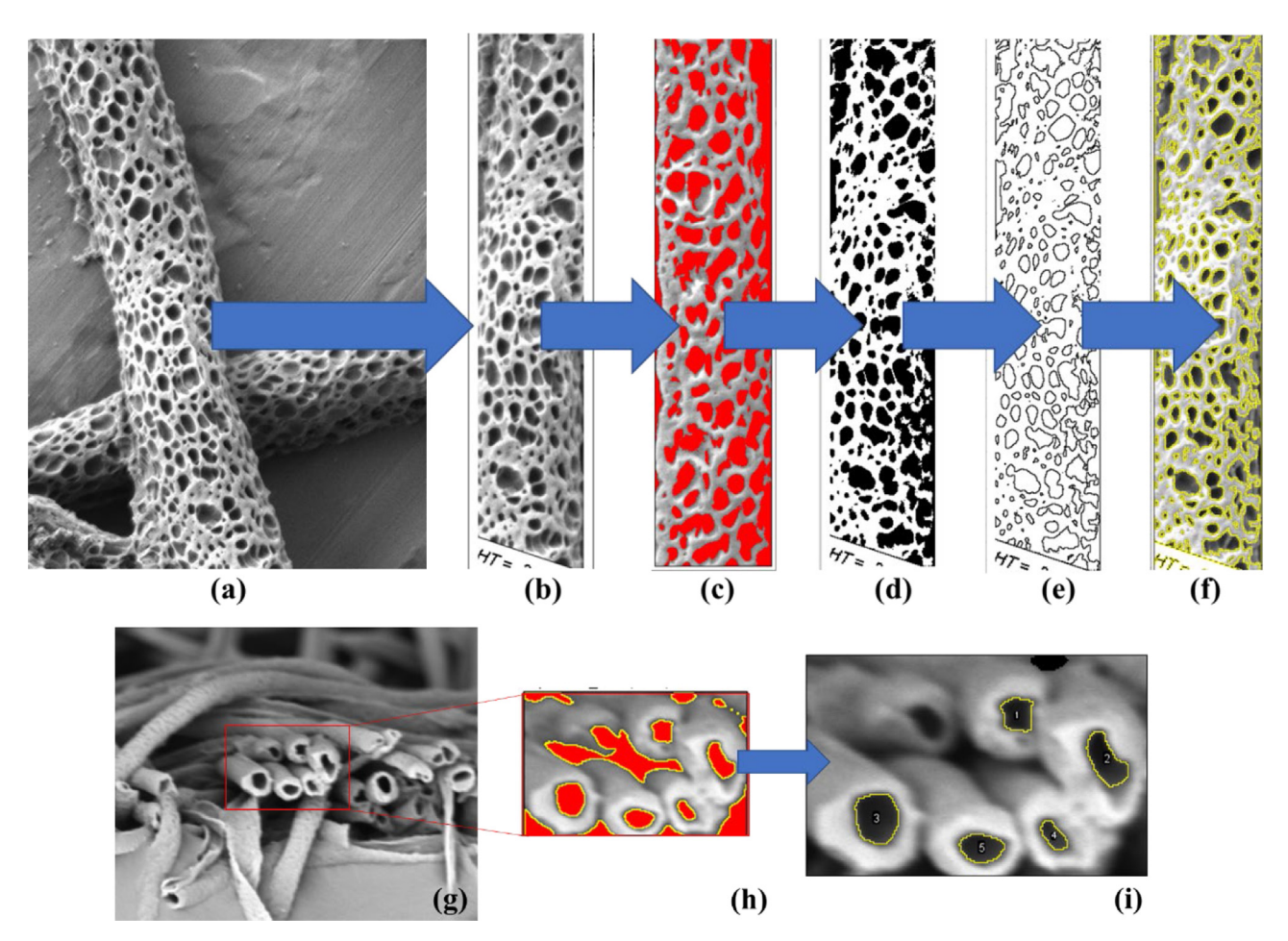


Fig. 6. The image processing steps for measuring pore and hollow cross-section size. (a) Raw SEM image (b) Region of Interest (ROI) selected and cropped (c) 8-bit contrast-based image thresholding (d) pixel masking (pore brightness intensity = 0). (e) pore area outline (f) boundary overlay on the original image. (g) selection of ROI on the original image (h) contrast-based thresholding (i) hollow area outline.

Fig. 6 shows the sequential steps used to process the surface pore area. After the final pore boundary was obtained, the individual pore area data was exported into a data frame. The noise in the images that appeared in the data frame was several orders of magnitude lower than the smallest visible pore. Prior to running the statistical analysis on the pore sizes, the noise data were filtered out as outliers.

3.3. Fiber morphology statistics

The fiber wall thickness was compared for all four CSVRs for each concentration configuration. Since the sample size for the wall thickness measurement was low (n = 15) and the normality of data distribution was not observed, we performed nonparametric statistical tests to compare the significance of the difference between groups. The results of the Wilcoxon test for each flowrate and concentration are demonstrated as boxplots in Fig. 7. The groups were color-coded. Different colors indicate that the groups are significantly different from each other. For all the configurations, the CSVR of 1:0.5 is significantly different from other CSVRs. For X1 and X3, three significantly different groups of wall thickness are observed (Fig. 7a and 7c). In those configurations, CSVRs of 1:1 and 1:2 fall within the same statistical groups. Alternatively, significant differences are observed in all CSVRs in both X2 and X4 as seen in Fig. 5b and 7d. In both cases, the core solution concentration changed is higher (6 % PEO in DCM). Also, the average wall thickness decreases as the core concentration increases for all CSVRs as seen from the comparison between Fig. 7c and 7d. Since no tubular structures are formed at a CSVR of 1:0.5 for configurations X1 and X3, the wall thickness values indicate the thickness of the open sheaths.

The boxplots for the fiber diameter at different CSVR and concentration configurations are shown in Fig. 8. The statistical significance in pair-wise comparison was determined by Wilcoxon nonparametric statistical testing. At CSVR 1:2 and 1:3, the microtube diameter falls in the range of 4-6 µm which is similar to that of human capillary vessels. We observe that the variation in core solution concentration alone results in three significantly different groups as seen in Fig. 8a and 8b. In these cases, CSVRs of 1:0.5 and 1:1 do not show a significant statistical difference in their average fiber diameter. With the increase in only the sheath solution concentration, significantly different groups of fiber diameters are observed across all CSVRs as seen in Fig. 8c and 8d. In this case, CSVRs of 1:0.5 and 1:1 show a significant difference in diameter for higher sheath concentration (12 % PCL in DCM). The outside diameter of the microtubes has a strong positive relationship with the sheath solution flow rate. It should be noted that diameter values for groups X1 and X3 at the CSVR of 1:0.5 were measured as the width of the open sheaths because there were no tubular structures in these settings.

The effect of core concentration on pore sizes for fixed sheath concentration and CSVR is shown in Fig. 9. Fig. 9a shows the result of the Mann-Whitney *U* test comparison of pore sizes in groups X3 and X4. No significant difference was observed with different core

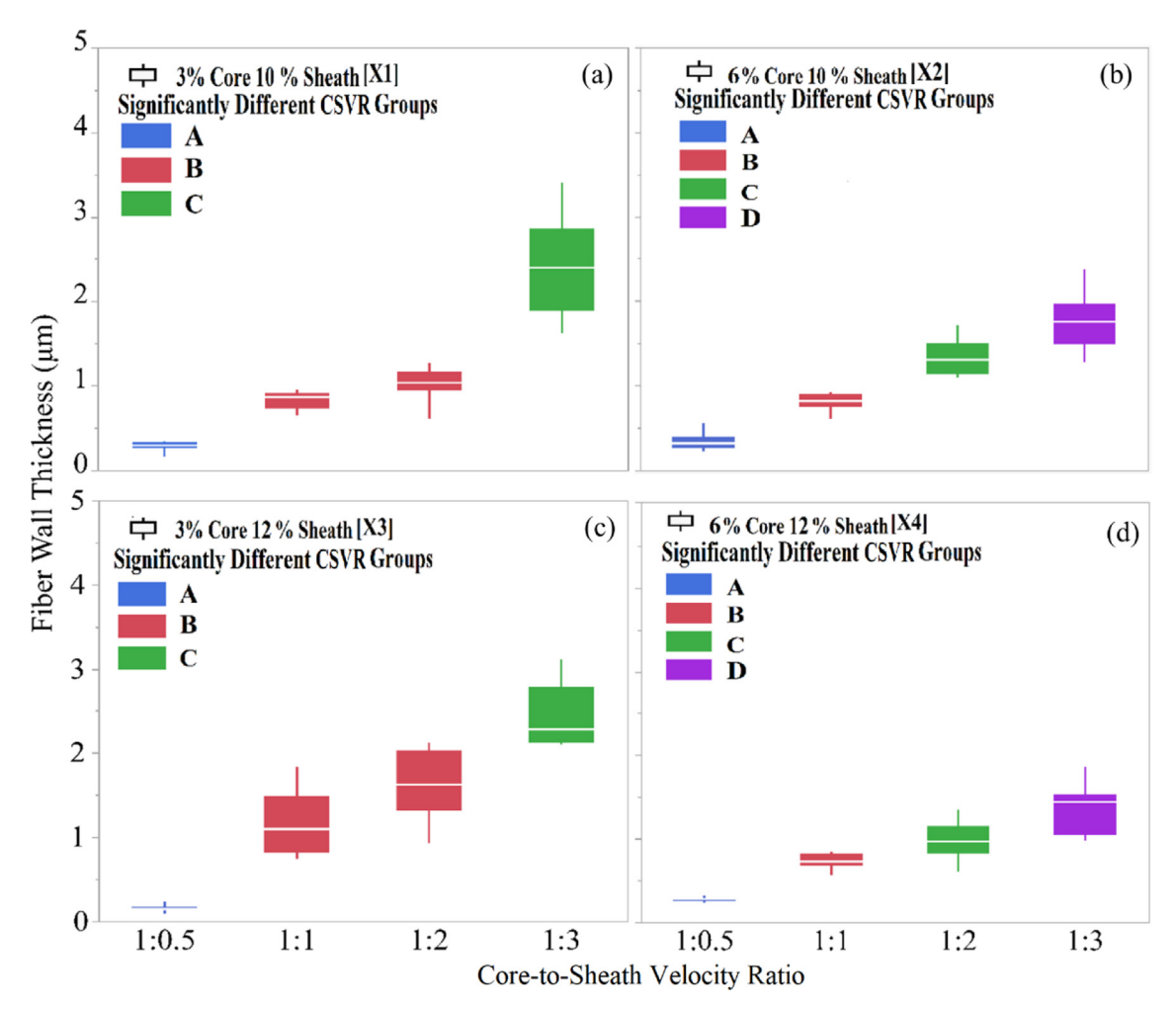


Fig. 7. CSVR effect on fiber wall thickness for the concentration configurations of (a) X1 (b) X2 (c) X3 (d) X4. Different colors indicate a significant statistical difference.

concentrations. Similarly, for CSVR of 1:3, no significant difference in pore area sizes was observed when the core solution concentration changed. Thus, the current results show that the change in core concentration does not have a significant effect on the pore size.

The effect of sheath concentration on pore size is demonstrated in Fig. 10. With a CSVR of 1:2 and a fixed core concentration, the pore sizes of X2 (10 % PCL) and X4 (12 % PCL) are compared in Fig. 10(a). Results of the Mann-Whitney U test show that there is a significant difference in the pore size area between the two groups. A similar trend is observed for X2 and X4 with a CSVR of 1:3 (P < 0.0001). The correlation between the pore size and sheath solution concentration has been reported in other studies [57]. With the increase in sheath solution concentration, the viscosity of the sheath polymer solution increases. The viscosity of the sheath solution has been identified as a driving factor for increased pore size in the core-sheath structure [58]. CSVRs of 1:0.5 and 1:1 were not used for comparisons as they do not form well-defined porous structures in concentration configurations of X1, X2, and

Fig. 11 illustrates the effect of CSVR on the pore size distribution. The pore sizes for different CSVRs in the concentration configurations of X2, X3, and X4 were compared using the Mann-Whitney *U* test (for groups of 2 in Fig. 11b and 11c) or Each-Pair Wilcoxon test (for a group of 4 in Fig. 9a) following a Kruskal-Wallis test. Fig. 11 shows that an increase in core/sheath CSVR results in larger pore sizes. The largest pore sizes are observed at

CSVR of 1:3. It is noted that lower CSVRs (1:0.5 and 1:1) are not shown for X3 and X2 because no well-defined porous structures were formed in those configurations. Furthermore, X1 did not demonstrate any porous structure at any CSVRs.

Other studies have shown that the dimension of the surface pores is strongly influenced by the evaporation time of the jet and the overall bulk polymer (both core and sheath) volume in the jet [59]. The diameter of the terminal jet before drying is proportionally related to the flow rate of the polymer solution [60,61]. With the increase in fiber diameter, hence larger fiber surface area, a larger amount of water molecules can condensate via the VIPS mechanism [62]. This eventually results in larger pore sizes with the increase in sheath solution flow rates.

The effects of CSVR, concentration, and viscosity ratio on the outside diameter, wall thickness, and hollow area percentage are illustrated using surface plots generated from multivariate linear regression with interaction models as shown in Fig. 12. The x-axis is the core-sheath viscosity ratio as shown in Table 3. Fig. 12a shows the combined effect of CSVR and viscosity ratio on the outside diameter. The regression model is as follows:

$$D = 2.21 - 0.69X_1 + 0.40X_2 + 0.29X_1X_2 \tag{3}$$

where D, X1, and X2 denote outside diameter, CSVR, and core-to-sheath viscosity. The R-square value is 92 % indicating a good fit for all the experimental values. For all viscosity ratios, CSVR level 1 has the lowest diameter with d < 2 μ m indicated by the deep blue color contour of the surface plot. CSVRs of 1:1 and 1:2

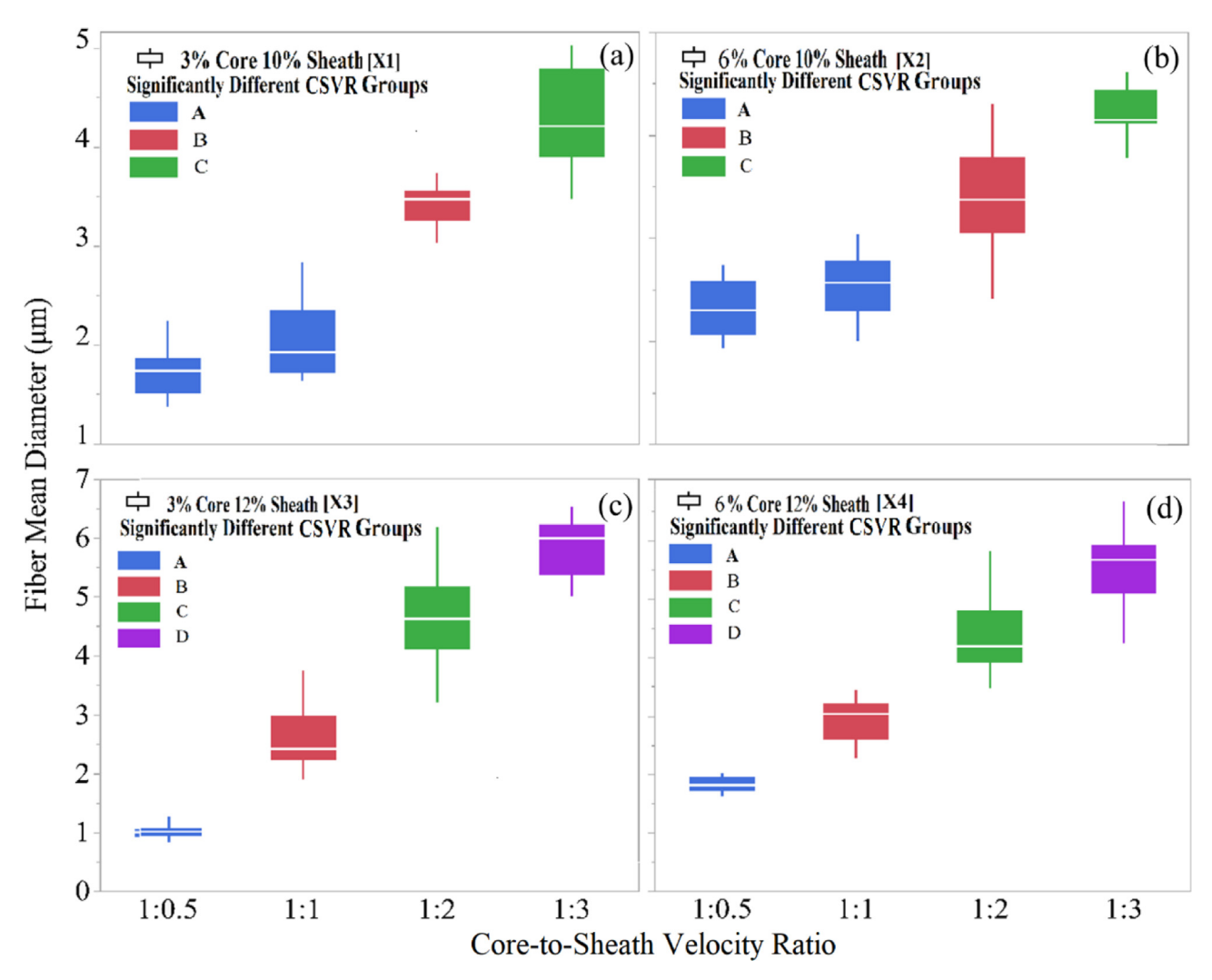


Fig. 8. The effect of CSVR on the mean diameter for concentration configurations of (a) X1 (b) X2 (c) X3 (d) X4. The statistical significance was color coded.

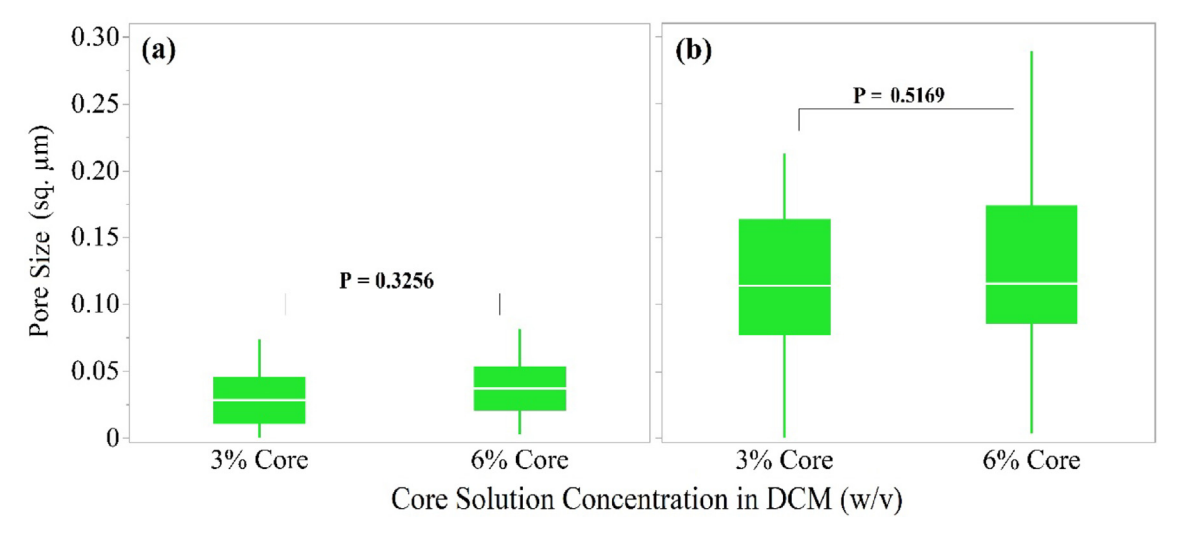


Fig. 9. Effect of core concentration change on pore size for CSVR of (a) 1:2 (b) 1:3.

show moderate diameter values with 2 $\mu m \le d \le 4 \mu m$ for all concentration configurations. The maximum range of diameter is obtained at CSVR level 4 (1:3), where all viscosity ratios result in diameters ranging from 4 μm to 6 μm . From Fig. 12a, we observed

that the peak value was obtained for the highest CSVR level 4 and highest sheath viscosity. This is because CSVR increases the Taylor

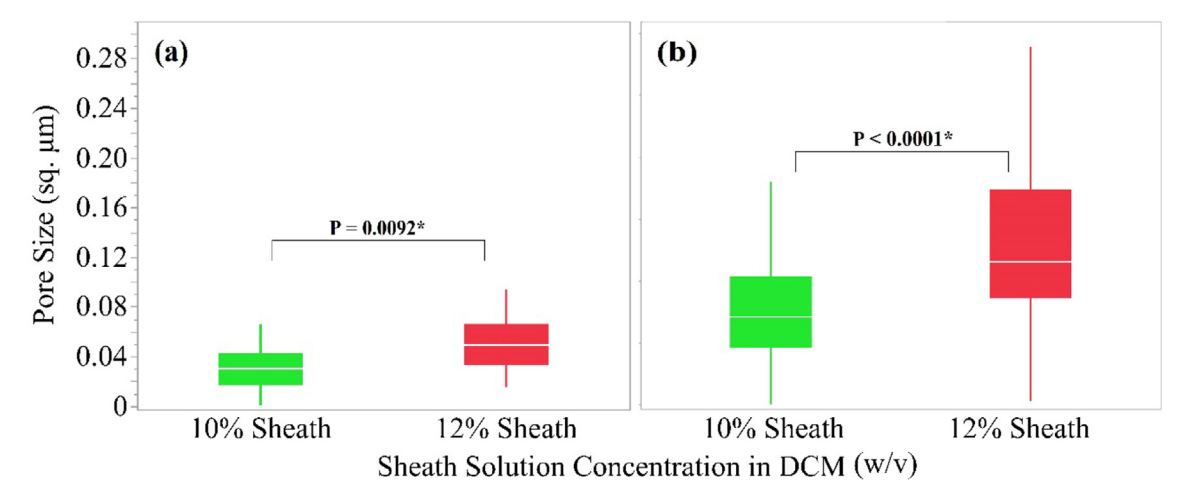


Fig. 10. Effect of Sheath concentration change on pore size for CSVR of (a) 1:2 (b) 1:3. Different colors indicate a significant statistical difference.

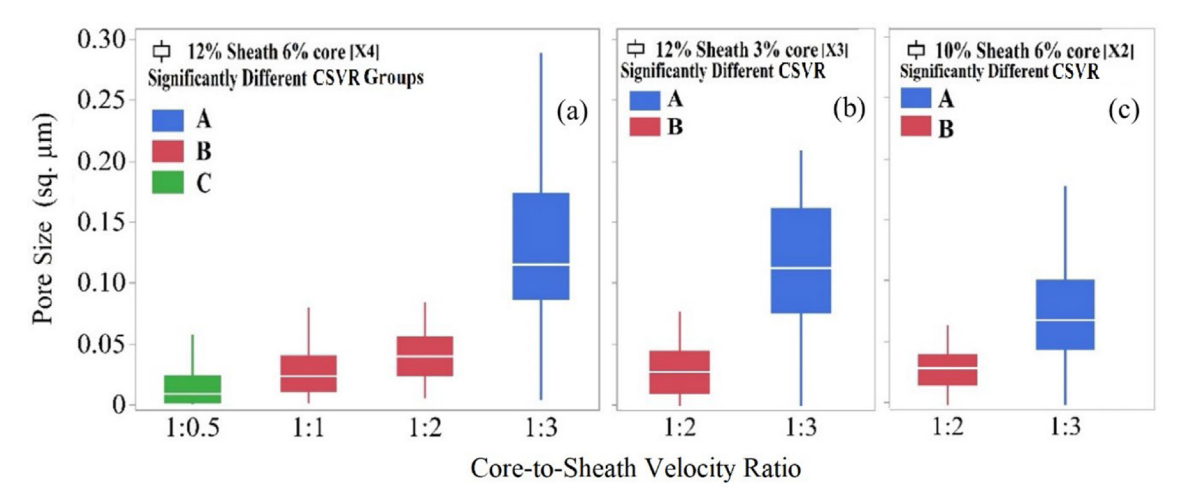


Fig. 11. Effect of CSVR on fiber surface pore size for concentration configuration of (a) X1 (b) X3 (c) X2. Different colors indicate a significant statistical difference.

cone size, jet diameter, and eventually the final fiber size [63]. The increased viscosity in the sheath solution results in a larger fiber diameter [63].

Fig. 12b demonstrates the fitted surface plot of the effect of concentration configuration and CSVR on the wall thickness of the microtubes. The model equation corresponding to the multivariate regression model is as follows:

$$W = 0.04 - 0.13X_1 + 0.30X_2 + 0.10X_1X_2 \tag{4}$$

where W represents the response variable wall thickness for X1 and X2. The R-square value is 90 % indicating the surface model represents the experimental data with good accuracy. We observe that the lowest at the lowest CSVR level 1 (1:0.5), the wall thickness is minimal with $t \leq 1~\mu m$ for all viscosity ratios. Consecutively, wall thickness increases as the CSVR is increased for all concentration configurations. The highest wall thickness is obtained at CSVR level 4 (1:3), and the core-to-sheath viscosity ratio is<1. This is indicated by the yellow color-contoured zone in Fig. 12b. In those regions of the 3D plot, the viscosity of the sheath is higher than that of the core. Thus, when sheath viscosity and velocity are 3x higher than the core, thick walls > 2 μm for the current experimental conditions.

The effects of CSVR and core-to-sheath viscosity ratio on the hollow cross-sectional area percentage are demonstrated in Fig. 12c. The hollow portion is calculated as the percentage of the

hollow area in the cross-sectional area of the microtube as demonstrated in Fig. 12d. The hollow portion percentage depends on the wall thickness and the outside diameter. The microtubes with the largest hollow portion percentage are formed below CSVR level 4 (1:3) at a core-to-sheath viscosity ratio ≤ 1 . In other words, the highest internal volume of the microtubes is obtained when the viscosity of the core is greater than or equal to that of the sheath solution. It should be noted that in Fig. 12c, not all experiment settings resulted in a tubular structure. The hollow portion values in these settings were assigned as 0 in the surface plots. The regression model is as follows:

$$H = -18.73 + 18.90X_1 + 7.32X_2 - 5.15X_1X_2$$
 (5)

where H denotes the percentage of the hollow portion area. The R-square value in Fig. 12c is 72 %. This is because we assigned a numerical value (0 %) to a physical phenomenon (open sheaths) for model-fitting purposes. This may be avoided by considering models with fully encapsulated sheaths only, and hence can be an area of improvement for future investigations.

4. Discussion

Artificial blood vessels play a critical role in the advancement of regenerative medicine. They provide oxygen and nutrients to engineered tissues, replace damaged or diseased natural blood vessels,

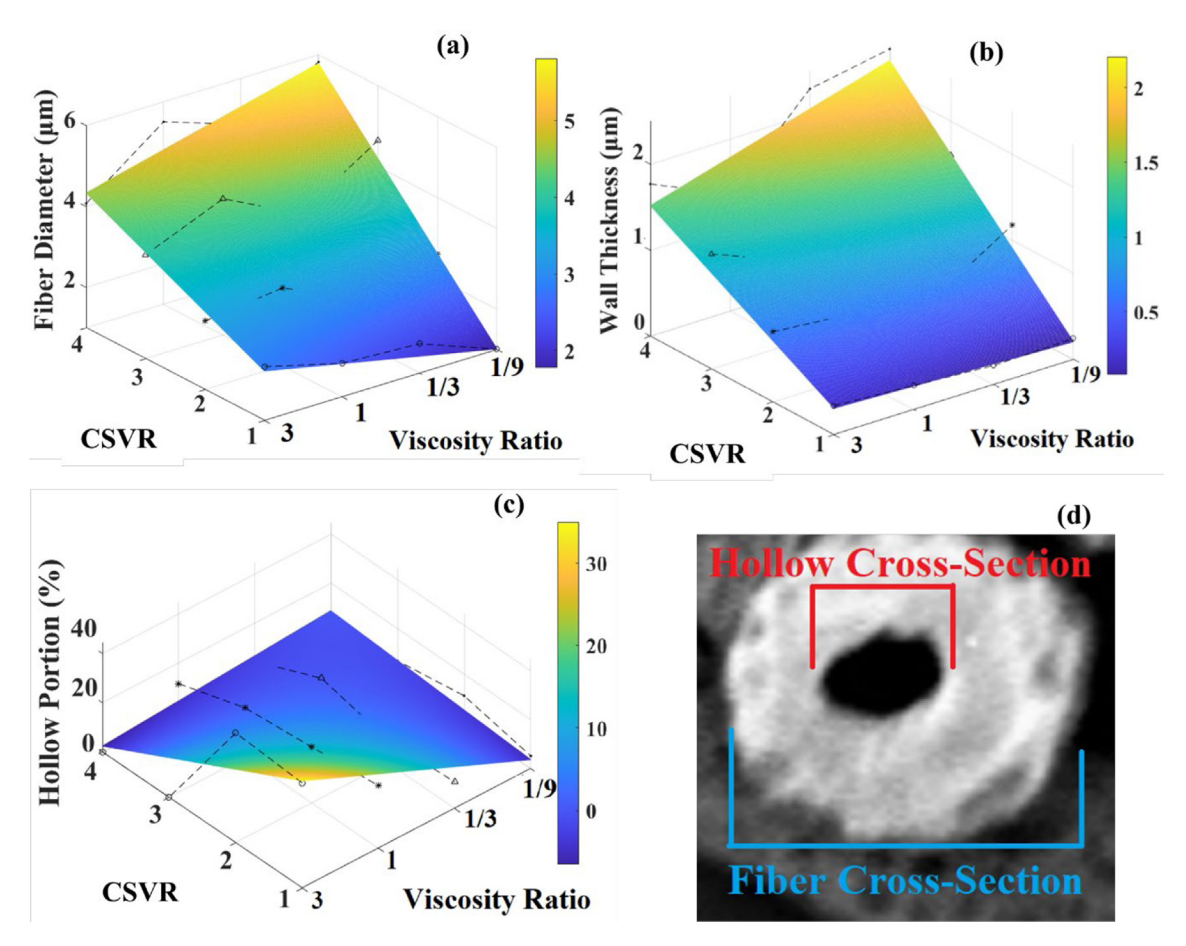


Fig. 12. Multivariate polynomial regression surface plot of (a) the CSVR and concentration on the outside diameter (b) the CSVR and concentration on the wall thickness (c) the CSVR and concentration on the hollow area. (d) An SEM image of the cross-section of a microtube.

and improve the survival and integration of transplanted tissues. They are also used to study disease in *in vitro* models of the circulatory system [64]. In tissue engineering, the integration of artificial blood vessels in cell-laden scaffolds will not only form temporary biodegradable channels for mass transport but also support and guide the attachment and migration of endothelial cells for vascularization [65,66]. Despite significant progress, most of the current manufacturing processes of artificial blood vessels are time-consuming and complex, requiring precise control of material properties and geometric parameters [64].

Decellularized allogenic or xenogenic grafts provide naturally and intact vascular conduits. The disadvantages lie in the difficulties of obtaining personalized organ scaffolds, limited types of organs, and potential disruption to the extracellular matrix (ECM). To promote the formation of a vascular network, various 2D and 3D models [67,68] were developed with structural and microenvironmental mimicry. Traditionally, sacrificial molds or inserts were used to create a tube network in 3D hydrogel scaffolds [69–72]. The latest strategies focus on one-step 3D printing vascular constructs [73–75]. Stereolithography can print vascular channels and lumen-like structures with high resolution and network geometries [76]. Microscale continuous digital light processing was able to fabricate tissues with gradient channel widths ranging from 50 μm to 250 μm [77]. Despite the high resolution, fabricating large scaffolds (centimeter-sized) with these techniques has been limited. It is difficult to spatiotemporally upscale these processes into a rapid fabrication system for tissue constructs of a clinically-relevant size. Electrospinning has been a popular choice for the fabrication of synthetic vascular scaffolds with diameters ranging from centimeters to millimeters [78–80]. Recent studies have shown rapid cellular regeneration and endothelization in single and multi-layered electrospun scaffolds [81–84]. These studies are based on traditional electrospinning method which spins the microfibers onto a mandrel to form a tubular shape [85–88]. This configuration is unable to fabricate capillary vasculatures, which have diameters ranging from 5 to 10 μ m.

Our study shows that vapor coaxial electrospinning has the capability to fabricate porous microtubes that closely resemble human capillary vessels. The microtube structure can be modulated by the solution concentrations and the flowrate of the core/sheath solutions. Future studies will focus on the microtubes' mechanical properties, including elasticity, tensile strength, burst pressure, and the in vitro capillary permeability of the nanoporous microtubes for mass transport.

5. Conclusion

Coaxial electrospinning is a highly efficient fabrication method for creating nanoporous microtubes as artificial capillaries. Understanding the effects of critical material and process parameters on the morphology of artificial capillaries is crucial for designing suitable biomimetic scaffolds for tissue vascularization. In this paper, we investigated the role of solution viscosity, solution surface tension, and flow velocity ratio in three major features of microtubes: outside diameter, wall thickness, and pore size. The outside diameters of the microtubes ranged from 2 to 5 μm . The wall thickness ranged from 0.5 to 2.5 μm . The average pore size ranged from 0.01 to 0.1 square μm . The analysis shows that the diameter and the

wall thickness are positively correlated with the sheath viscosity and sheath flow rate. The core solution only affects the outside diameter but does not influence the pore size. Polynomial regression models were generated to quantify the effects. Based on the models, the viscosity of the sheath solution needs to be greater or equal to that of the core solution to generate a tubular structure. Meanwhile, the surface tensions of the core and sheath solutions need to be substantially different to avoid a homogeneous mixture and maintain a concentric structure during the electrospinning. It is also desirable to keep the flow velocity of the core solution equal to or higher than that of the sheath solution. In addition, surface pores are formed at high sheath solution concentrations and high sheath volumetric flow rates. The pore size is positively correlated to the sheath volumetric flow rate. Overall, the findings from this paper provide a guideline for electrospinning nanoporous microtubes with tunable morphological features that serve as capillary vessels for tissue engineering.

Data availability

Data will be made available on request.

Declaration of Competing Interest

The authors declare the following financial interests/personal relationships which may be considered as potential competing interests: [George Tan reports financial support was provided by National Science Foundation.].

Acknowledgment

This work was supported by the National Science Foundation under grant number CMMI-2145108.

Appendix A. Supplementary data

Supplementary data to this article can be found online at https://doi.org/10.1016/j.matdes.2023.111708.

References

- D. Seliktar, D. Dikovsky, E. Napadensky, Bioprinting and tissue engineering: recent advances and future perspectives, Israel Journal of Chemistry 53 (9–10) (2013) 795–804.
- [2] B. Schmidt-Nielsen, August Krogh and capillary physiology, International Journal of Microcirculation 14 (1–2) (1994) 104–110.
- [3] T. Kaully et al., Vascularization—the conduit to viable engineered tissues, Tissue Engineering Part B: Reviews 15 (2) (2009) 159–169.
- [4] F.A. Auger, L. Gibot, D. Lacroix, The pivotal role of vascularization in tissue engineering, Annu Rev Biomed Eng 15 (1) (2013) 177–200.
- [5] Y. Zhang et al., Recent advances in 3D bioprinting of vascularized tissues, Materials & Design 199 (2021) 109398.
- [6] P. Zhuang et al., Bioprinting of 3D in vitro skeletal muscle models: A review, Materials & Design 193 (2020) 108794.
- [7] H. Ma et al., Integrated design and fabrication strategies based on bioprinting for skeletal muscle regeneration: current status and future perspectives, Materials & Design (2023) 111591.
- [8] W. Jia et al., Direct 3D bioprinting of perfusable vascular constructs using a blend bioink, Biomaterials 106 (2016) 58–68.
- [9] G. Gao et al., Tissue engineered bio-blood-vessels constructed using a tissue-specific bioink and 3D coaxial cell printing technique: a novel therapy for ischemic disease, Advanced functional materials 27 (33) (2017) 1700798.
- [10] W. Liu et al., Coaxial extrusion bioprinting of 3D microfibrous constructs with cell-favorable gelatin methacryloyl microenvironments, Biofabrication 10 (2) (2018) 024102.
- [11] A. Thomas et al., Vascular bioprinting with enzymatically degradable bioinks via multi-material projection-based stereolithography, Acta Biomaterialia 117 (2020) 121–132.
- [12] L.M. Kalossaka et al., 3D printing nanocomposite hydrogels with lattice vascular networks using stereolithography, Journal of Materials Research 36 (2021) 4249–4261.

[13] T. Ching, Y.-C. Toh, M. Hashimoto, Fabrication of complex 3D fluidic networks via modularized stereolithography, Advanced Engineering Materials 22 (3) (2020) 1901109.

- [14] Y.T. Kim et al., Additive manufacturing of a 3D vascular chip based on cytocompatible hydrogel, European Polymer Journal 151 (2021) 110451.
- [15] B. Souquet et al., Manufacturing a bone marrow-On-A-Chip using maskless photolithography, in: Bone Marrow Environment: Methods and Protocols, Springer, 2021, pp. 263–278.
- [16] D.G. Kasi et al., Rapid Prototyping of Organ-on-a-Chip Devices Using Maskless Photolithography, Micromachines 13 (1) (2021) 49.
- [17] S. Pradhan et al., Biofabrication strategies and engineered in vitro systems for vascular mechanobiology, Advanced healthcare materials 9 (8) (2020) 1901255.
- [18] A. Aazmi et al., Engineered vasculature for organ-on-a-chip systems, Engineering 9 (2022) 131–147.
- [19] B. Baddal, Microfluidic Organ-Chips and Infectious Diseases: Insights from the Development and Applications Perspective, Cyprus Journal of Medical Sciences 7 (1) (2022) 1–9.
- [20] K. Thakare et al., Bioprinting of organ-on-chip systems: a literature review from a manufacturing perspective, Journal of Manufacturing and Materials Processing 5 (3) (2021) 91.
- [21] F. Sima et al., 3D Biomimetic Chips for Cancer Cell Migration in Nanometer-Sized Spaces Using "Ship-in-a-Bottle" Femtosecond Laser Processing, ACS Applied Bio Materials 1 (5) (2018) 1667–1676.
- [22] Horng, H., et al. Biomimetic Microvascular Tissue Phantoms Fabricated with Two-Photon 3D Printing. in Frontiers in Optics. 2018. Optical Society of America.
- [23] W. Meyer et al., Soft polymers for building up small and smallest blood supplying systems by stereolithography, Journal of functional biomaterials 3 (2) (2012) 257–268.
- [24] R. Gao et al., Artificial Blood Vessel Frameworks from 3D Printing-Based Super-Assembly as In Vitro Models for Early Diagnosis of Intracranial Aneurysms, Chemistry of Materials 32 (7) (2020) 3188–3198.
- [25] J. Liu et al., Dual-gel 4D printing of bioinspired tubes, ACS applied materials & interfaces 11 (8) (2019) 8492–8498.
- [26] A. Kirillova et al., 4D biofabrication using shape-morphing hydrogels, Advanced Materials 29 (46) (2017) 1703443.
- [27] S. Ramakrishna, An introduction to electrospinning and nanofibers, World scientific, 2005.
- [28] J.J. Liu et al., Peripheral nerve regeneration using composite poly (lactic acid-caprolactone)/nerve growth factor conduits prepared by coaxial electrospinning, Journal of biomedical materials research Part A 96 (1) (2011) 13–20.
- [29] H. Yoshimoto et al., A biodegradable nanofiber scaffold by electrospinning and its potential for bone tissue engineering, Biomaterials 24 (12) (2003) 2077–2082.
- [30] M.R. Ladd et al., Co-electrospun dual scaffolding system with potential for muscle-tendon junction tissue engineering, Biomaterials 32 (6) (2011) 1549– 1559.
- [31] X. Zong et al., Electrospun fine-textured scaffolds for heart tissue constructs, Biomaterials 26 (26) (2005) 5330–5338.
- [32] C. Vaz et al., Design of scaffolds for blood vessel tissue engineering using a multi-layering electrospinning technique, Acta biomaterialia 1 (5) (2005) 575–582.
- [33] A. Moghe, B. Gupta, Coaxial electrospinning for nanofiber structures: preparation and applications, Polymer Reviews 48 (2) (2008) 353–377.
- [34] H. Jiang, L. Wang, K. Zhu, Coaxial electrospinning for encapsulation and controlled release of fragile water-soluble bioactive agents, Journal of Controlled Release 193 (2014) 296–303.
- [35] Y. Zhou, G.Z. Tan, Core-sheath wet electrospinning of nanoporous polycaprolactone microtubes to mimic fenestrated capillaries, Macromolecular Materials and Engineering 305 (7) (2020) 2000180.
- [36] Y. Zhou, I. Qavi, G.Z. Tan, Effects of Solution Viscosity on Poly (I-Lactic Acid) Porous Microtubes Fabricated by Core-Sheath Electrospinning, Journal of Micro and Nano-Manufacturing 9 (2) (2021).
 [37] Y. Zhou, D. Sooriyaarachchi, G.Z. Tan, Fabrication of nanopores polylactic acid
- [37] Y. Zhou, D. Sooriyaarachchi, G.Z. Tan, Fabrication of nanopores polylactic acid microtubes by core-sheath electrospinning for capillary vascularization, Biomimetics 6 (1) (2021) 15.
- [38] D. Sooriyaarachchi, S. Maharubin, G.Z. Tan, Fabrication of Microtube-Embedded Chip to Mimic Blood-Brain Barrier Capillary Vessels, in: The Blood-Brain Barrier, Springer, 2022, pp. 241–249.
- [39] D.H. Reneker et al., Bending instability of electrically charged liquid jets of polymer solutions in electrospinning, Journal of Applied physics 87 (9) (2000) 4531–4547.
- [40] A.C. Stijnman, I. Bodnar, R.H. Tromp, Electrospinning of food-grade polysaccharides, Food Hydrocolloids 25 (5) (2011) 1393–1398.
- [41] J.H. Park, G.C. Rutledge, Ultrafine high performance polyethylene fibers, Journal of Materials Science 53 (4) (2018) 3049–3063.
- [42] S. Wan et al., Pendant Drop Method for Interfacial Tension Measurement Based on Edge Detection, IEEE, 2009.
- [43] F. Hansen, G. Rødsrud, Surface tension by pendant drop: I. A fast standard instrument using computer image analysis, Journal of colloid and interface science 141 (1) (1991) 1–9.
- [44] P. Gupta et al., Electrospinning of linear homopolymers of poly (methyl methacrylate): exploring relationships between fiber formation, viscosity, molecular weight and concentration in a good solvent, Polymer 46 (13) (2005) 4799–4810.

- [45] L. Du et al., Electrospinning of polycaprolatone nanofibers with DMF additive: The effect of solution proprieties on jet perturbation and fiber morphologies, Fibers and Polymers 17 (5) (2016) 751–759.
- [46] S.C. Ayirala, D.N. Rao, Solubility, miscibility and their relation to interfacial tension in ternary liquid systems, Fluid phase equilibria 249 (1–2) (2006) 82–91.
- [47] Z. Kurban et al., A solution selection model for coaxial electrospinning and its application to nanostructured hydrogen storage materials, The Journal of Physical Chemistry C 114 (49) (2010) 21201–21213.
- [48] T.T.T. Nguyen, O.H. Chung, J.S. Park, Coaxial electrospun poly (lactic acid)/chitosan (core/shell) composite nanofibers and their antibacterial activity, Carbohydrate Polymers 86 (4) (2011) 1799–1806.
- [49] N. Kaerkitcha et al., Influence of the viscosity ratio of polyacrylonitrile/poly (methyl methacrylate) solutions on core-shell fibers prepared by coaxial electrospinning, Polymer journal 49 (6) (2017) 497–502.
- [50] D. Li, Y. Xia, Direct fabrication of composite and ceramic hollow nanofibers by electrospinning, Nano letters 4 (5) (2004) 933–938.
- [51] H. Cheng et al., Biomedical application and controlled drug release of electrospun fibrous materials, Materials Science and Engineering: C 90 (2018) 750–763.
- [52] D. Mailley, A. Hebraud, G. Schlatter, A review on the impact of humidity during electrospinning: From the nanofiber structure engineering to the applications, Macromolecular Materials and Engineering 306 (7) (2021) 2100115.
- [53] L. Pauchard, C. Allain, Buckling instability induced by polymer solution drying, EPL (Europhysics Letters) 62 (6) (2003) 897.
- [54] C.-L. Pai, M.C. Boyce, G.C. Rutledge, Morphology of porous and wrinkled fibers of polystyrene electrospun from dimethylformamide, Macromolecules 42 (6) (2009) 2102–2114.
- [55] P.K. Szewczyk, U. Stachewicz, The impact of relative humidity on electrospun polymer fibers: From structural changes to fiber morphology, Advances in Colloid and Interface Science 286 (2020) 102315.
- [56] A. Haider, S. Haider, I.-K. Kang, A comprehensive review summarizing the effect of electrospinning parameters and potential applications of nanofibers in biomedical and biotechnology, Arabian Journal of Chemistry 11 (8) (2018) 1165–1188
- [57] J. Zheng et al., Construction of hierarchical structures by electrospinning or electrospraying, Polymer 53 (2) (2012) 546–554.
- [58] G.H. Lee, J.-C. Song, K.-B. Yoon, Controlled wall thickness and porosity of polymeric hollow nanofibers by coaxial electrospinning, Macromolecular Research 18 (6) (2010) 571–576.
- [59] T.T.T. Nguyen et al., Porous core/sheath composite nanofibers fabricated by coaxial electrospinning as a potential mat for drug release system, International journal of pharmaceutics 439 (1–2) (2012) 296–306.
- [60] S.V. Fridrikh et al., Controlling the fiber diameter during electrospinning, Physical review letters 90 (14) (2003) 144502.
- [61] T. Subbiah et al., Electrospinning of nanofibers, Journal of applied polymer science 96 (2) (2005) 557–569.
- [62] M. Şimşek, Tuning surface texture of electrospun polycaprolactone fibers: Effects of solvent systems and relative humidity, Journal of Materials Research 35 (3) (2020) 332–342.
- [63] B. Pant, M. Park, S.-J. Park, Drug delivery applications of core-sheath nanofibers prepared by coaxial electrospinning: a review, Pharmaceutics 11 (7) (2019) 305
- [64] S. Fleischer, D.N. Tavakol, G. Vunjak-Novakovic, From arteries to capillaries: approaches to engineering human vasculature, Advanced functional materials 30 (37) (2020) 1910811.
- [65] J. Zhou et al., Dual layer collagen-GAG conduit that mimic vascular scaffold and promote blood vessel cells adhesion, proliferation and elongation, Materials Science and Engineering: C 92 (2018) 447–452.

- [66] D. Lei et al., 3D printing of biomimetic vasculature for tissue regeneration, Materials Horizons 6 (6) (2019) 1197–1206.
- [67] G. Gillispie et al., Assessment methodologies for extrusion-based bioink printability, Biofabrication 12 (2) (2020) 022003.
- [68] S. Naghieh, X. Chen, Printability—A key issue in extrusion-based bioprinting, Journal of Pharmaceutical Analysis 11 (5) (2021) 564–579.
- [69] D.B. Kolesky et al., 3D bioprinting of vascularized, heterogeneous cell-laden tissue constructs, Advanced materials 26 (19) (2014) 3124–3130.
- [70] V.K. Lee et al., Creating perfused functional vascular channels using 3D bioprinting technology, Biomaterials 35 (28) (2014) 8092–8102.
- [71] A.C. Daly et al., 3D printed microchannel networks to direct vascularisation during endochondral bone repair, Biomaterials 162 (2018) 34–46.
- [72] R. Pimentel et al., Three-dimensional fabrication of thick and densely populated soft constructs with complex and actively perfused channel network, Acta biomaterialia 65 (2018) 174–184.
- [73] R. Xie et al., Engineering of hydrogel materials with perfusable microchannels for building vascularized tissues, Small 16 (15) (2020) 1902838.
- [74] C. Cui et al., 4D printing of self-folding and cell-encapsulating 3D microstructures as scaffolds for tissue-engineering applications, Biofabrication 12 (4) (2020) 045018.
- [75] T.T. Dang et al., Coaxial printing of double-layered and free-standing blood vessel analogues without ultraviolet illumination for high-volume vascularised tissue, Biofabrication 12 (4) (2020) 045033.
- [76] I. Orellano et al., Engineering Vascular Self-Assembly by Controlled 3D-Printed Cell Placement, Advanced Functional Materials 32 (52) (2022) 2208325.
- [77] H. Goodarzi Hosseinabadi et al., Digital light processing bioprinting advances for microtissue models, ACS Biomaterials Science & Engineering 8 (4) (2022) 1381–1395.
- [78] Q. Hu et al., Designed and fabrication of triple-layered vascular scaffold with microchannels, Journal of Biomaterials Science, Polymer Edition 32 (6) (2021) 714–734.
- [79] E. Tolba, Diversity of electrospinning approach for vascular implants: multilayered tubular scaffolds, Regenerative Engineering and Translational Medicine 6 (2020) 383–397.
- [80] F. Liu et al., Poly (l-lactide-co-caprolactone)/tussah silk fibroin nanofiber vascular scaffolds with small diameter fabricated by core-spun electrospinning technology, Journal of Materials Science 55 (2020) 7106–7119.
- [81] D. Chen et al., Shapeable large-pore electrospun polycaprolactam cotton facilitates the rapid formation of a functional tissue engineered vascular graft, Materials & Design 191 (2020) 108631.
- [82] Y. Wang et al., A bilayer vascular scaffold with spatially controlled release of growth factors to enhance in situ rapid endothelialization and smooth muscle regeneration, Materials & Design 204 (2021) 109649.
- [83] D. Jin et al., Preliminary application of a cell-free mono-layered vascular scaffold in a rabbit model, Materials & Design 198 (2021) 109301.
- [84] M.A. Al Fahad et al., Endothelialization and smooth muscle cell regeneration capabilities of a bi-layered small diameter vascular graft for blood vessel reconstruction, Materials & Design 225 (2023) 111488.
- [85] S. Park et al., Fabrication of strong, bioactive vascular grafts with PCL/collagen and PCL/silica bilayers for small-diameter vascular applications, Materials & Design 181 (2019) 108079.
- [86] S. Najafi, A. Gharehaghaji, S. Etrati, Fabrication and characterization of elastic hollow nanofibrous PU yarn, Materials & Design 99 (2016) 328–334.
- [87] A.P. Rickel et al., Electrospun nanofiber scaffold for vascular tissue engineering, Materials Science and Engineering: C 129 (2021) 112373.
- [88] I. Woods et al., Fabrication of blood-derived elastogenic vascular grafts using electrospun fibrinogen and polycaprolactone composite scaffolds for paediatric applications, Journal of Tissue Engineering and Regenerative Medicine 14 (9) (2020) 1281–1295.